RSC Advances

PAPER

View Article Online
View Journal | View Issue

Cite this: *RSC Adv.*, 2022, **12**, 4562

Enhanced phosphate removal with fine activated alumina synthesized from a sodium aluminate solution: performance and mechanism

Guoyu Wu,[ab] Guihua Liu,*[a] Xiaobin Li,[a] Zhihong Peng,[a] Qiusheng Zhou[a] and Tiangui Qi[a]

Fine activated alumina (FAA) acting as an adsorbent for phosphate was synthesized from an industrial sodium aluminate solution based on phase evolution from $Al(OH)_3$ and $NH_4Al(OH)_2CO_3$. This material was obtained in the form of γ-Al_2O_3 with an open mesoporous structure and a specific surface area of 648.02 $m^2\ g^{-1}$. The phosphate adsorption capacity of the FAA gradually increased with increases in phosphate concentration or contact time. The maximum adsorption capacity was 261.66 mg g^{-1} when phosphate was present as $H_2PO_4^-$ at a pH of 5.0. A removal efficiency of over 96% was achieved in a 50 mg L^{-1} phosphate solution. The adsorption of phosphate anions could be explained using non-linear Langmuir or Freundlich isotherm models and a pseudo-second-order kinetic model. Tetra-coordinate AlO_4 sites acting as Lewis acids resulted in some chemisorption, while $(O)_nAl(OH)_2^+$ (n = 4, 5, 6) Brønsted acid groups generated by the protonation of AlO_4 or AlO_6 sites in the FAA led to physisorption. Analyses of aluminum-oxygen coordination units using Fourier transform infrared and X-ray photoelectron spectroscopy demonstrated that physisorption was predominant. Minimal chemisorption was also verified by the significant desorption rate observed in dilute NaOH solutions and the high performance of the regenerated FAA. The high specific surface area, many open mesopores and numerous highly active tetra-coordinate AlO_4 sites on the FAA all synergistically contributed to its exceptional adsorption capacity.

Received 19th November 2021
Accepted 24th January 2022

DOI: 10.1039/d1ra08474g

rsc.li/rsc-advances

1. Introduction

Wastewater containing high concentrations of phosphate as a pollutant can be generated as a result of papermaking, the use of phosphorus-based fertilizers and the surface treatment of metals. This is problematic because excessive amounts of phosphate in aquatic systems lead to serious water pollution effects, such as eutrophication and algae bloom.[1] Traditionally, phosphate has been removed from wastewater by chemical precipitation, crystallization, ion exchange, electrostatic techniques, hydrobiological processes and adsorption.[2–4] Among these, adsorption methods have been widely adopted because of their operational simplicity, and excellent treatment efficient, and the adsorbents can be regenerated in some cases. The adsorbents used to date include natural minerals, industrial slag and synthetic materials. However, the use of natural minerals such as bentonite, attapulgite and kaolin or industrial slag (such as red mud) are limited by the low adsorption capacity of these substances (8–56 mg g^{-1}), the large amount of sludge they generate and the potential for secondary pollution. In addition, synthetic inorganic adsorbents (including iron oxide, titanium oxide, cerium oxide, water talc, and calcined layered materials) are difficult to prepare and are also not readily regenerated. Activated alumina, serving as a replacement for α-Al_2O_3, is considered a promising inorganic adsorbent because it provides numerous active sites for highly efficient phosphate adsorption and is also inexpensive, stable and environmentally-friendly.[5–8] As a consequence of these attributes, the use of activated alumina has been widely studied. Even so, conventional fine activated alumina (FAA) with a medium particle size of $d(50) > 1$ μm has been found to exhibit a low adsorption capacity (30.2 mg g^{-1}) as a result of its minimal specific surface area (less than 300 $m^2\ g^{-1}$).[9] Therefore, both nano-$Al(OH)_3$ and nano-AlOOH have been used as precursor to synthesize nano-alumina as a means of increasing the specific surface area, leading to an improved values from 300 to 600 $m^2\ g^{-1}$.[10] The phosphate adsorption capacity of this nanoscale material was determined to be 31.1–102 mg g^{-1} when applied to solutions containing phosphate concentrations ranging from 50 to 1400 mg L^{-1}. However, the preparation of the nano-alumina from aluminum-bearing salts ($Al_2(SO_4)_3$ $Al(NO_3)_3$, $AlCl_3$) and aluminum alkoxides ($Al(OR)_3$) as raw materials is difficult because the resulting nanoparticles tend to undergo significant aggregation and because a considerable

[a]School of Metallurgy and Environment, Central South University, Changsha 410083, Hunan, China. E-mail: liugh303@csu.edu.cn
[b]Changchun Gold Research Institute Co., Ltd, Changchun 130012, Jilin, China

amount of saline wastewater is produced in conjunction with the use of alkaline reagents. By contrast, gibbsite or boehmite precipitated from industrial sodium aluminate solution generated in alumina refineries is remarkably inexpensive and has a minimal negative environmental impact because this process allows the sodium aluminate solution to be recycled and does not generate wastewater.[11] This method therefore represents a green, economical approach to synthesizing FAA having a high specific surface area (>300 $m^2\ g^{-1}$) as an alternative to nano-alumina.

To date, various isotherm and kinetic models have been employed to assess phosphate removal mechanisms. Specifically, the Langmuir, Freundlich, Tempkin, and Dubinin–Radushkevich isotherm models have all been applied to assess the adsorption of phosphate anions on alumina surfaces.[12–14] In addition, pseudo-first-order, pseudo-second-order and Elovich kinetic models have also been adopted.[15] Simulations of the distribution of various phosphate and Al^{3+} species in solution at different pH values have indicated that $AlPO_4$ might be formed on alumina surfaces.[3,16–18] Furthermore, Fourier-transform infrared (FTIR) spectroscopy, X-ray photoelectron spectroscopy (XPS) and zeta potential measurements have all been used to study the interactions between phosphate anions and alumina as well as to examine physisorption or chemisorption processes.[19] Nevertheless, the interactions of phosphate anions with FAA have not determined.

The adsorption properties of activated alumina are primarily the result of active sites on the material. Compared with α-Al_2O_3, which is inert and almost completely composed of hexacoordinated AlO_6, various other aluminum–oxygen coordination units (AlO_x where $x = 4$ or 5) may occur in the activated alumina, leading to catalytic activity.[20] These observations may assist in determining the mechanism by which this material removes phosphate from wastewater and may also help to optimize the process. Therefore, in addition to distribution of Al–O units, the interactions between phosphate anions and AlO_4, AlO_5 and AlO_6 units in activated alumina are expected to affect adsorption properties.

The present work evaluated the phosphate removal performance of FAA and explored the associated mechanism. FAA having a high specific surface area was prepared by phase evolution from gibbsite and characterized with regard to its particle size distribution (PSD) and using X-ray diffraction (XRD), N_2 adsorption–desorption isotherms analyses and scanning electron microscopy (SEM). The phosphate adsorption isotherm and kinetics of this material were then studied based on batch experiments while the removal mechanism was investigated using zeta potential measurements, FTIR spectroscopy and XPS. The resulting data were used to determine the AlO_4 and AlO_6 distribution in the FAA before and after phosphate adsorption as a means of evaluating the adsorption mechanism. The data from this work offer an improved understanding of the adsorption properties of the activated alumina and could lead to optimization of phosphate removal from wastewater with this material.

2. Materials and experiment

2.1 Synthesis of FAA with high specific surface area

The adsorbent FAA was prepared according to our previous work[21] as follows: 15 mL of industrial sodium aluminate solution ($C_{Na_2O} = 2.26$ mol L^{-1}, $C_{Al_2O_3} = 1.57$ mol L^{-1}) and 400 mL of deionized water were added into a round flask, and 25 mL of H_2O_2 (10 wt%) was then added at 5 mL min^{-1} to generate $Al(OH)_3$ seed in vigorous agitation (1000 rpm), followed by precipitation of the $Al(OH)_3$ at 50 °C for 60 min. The fine $Al(OH)_3$ was filtered and washed with boiling deionized water. Afterwards, the fine $Al(OH)_3$ was placed into a flask containing 100 mL of $(NH_4)_2CO_3$ (1.54 mol L^{-1}) solution and 100 mL of deionized water. Meanwhile, ammonia (30 wt%) was added to adjust the solution pH to 10.0 with continuously stirring for 24 h to ensure the fine $Al(OH)_3$ transformed into $NH_4Al(OH)_2CO_3$. The resultant $NH_4Al(OH)_2CO_3$ were washed with deionized water until neutral pH (~7.0), and air-dried at 60 °C for 12 h. Finally, the XRD pattern and SEM image of the γ-Al_2O_3 (PDF No. 04-0880) used in this work are provided in Fig. 1. The XRD data indicate that received in a poor crystal for the dispersing diffraction peaks after $NH_4Al(OH)_2CO_3$ was roasted at 450 °C for 180 min. The average crystallite size in the sample was calculated using the Scherrer equation based on the (100) peak in the XRD pattern and determined to be 6.689 nm.[22] Meanwhile, the SEM image demonstrates that the FAA particles were in the form of short fibers having long spindle-like morphologies, with lengths of approximately 1.50 μm and diameters of approximately 0.25 μm (Fig. 1(b)). This image confirms that the γ-Al_2O_3 comprised a fine powder formed by the agglomeration of a large number of nanoparticles.

Fig. 2(a) presents the N_2 adsorption–desorption isotherms obtained from this material, which exhibit hysteresis loops in the relative pressure range of $0.4 < P/P_0 < 0.7$ and $P/P_0 > 0.9$. There loops are attributed to capillary condensation. These isotherms curve are generally consistent with the type IV category and have type H1 hysteresis loops according to the IUPAC classification system, and these results indicate that narrow slit-like open mesopores were primarily contained in the FAA.[21] Furthermore, the Brunauer–Emmett–Teller surface area of the FAA reached up to 648.02 $m^2\ g^{-1}$, and so was slightly higher than the values reported for nano-alumina prepared from aerogels or chemical evaporation and was significantly more than the values of 100 to 400 $m^2\ g^{-1}$ determined for superfine alumina with a $d(50)$ of 0.5 μm.[23,24] Fig. 2(b) shows that the material contained meso-pore and macro-pore with sizes in the ranges of 30–40 nm and 150–600 nm, respectively. The numerous meso-pores and smaller number of macro-pores in the FAA would be expected to promote its functioning as an adsorbent by providing pathways for the efficient transport of molecules.[25]

2.2 Adsorption of phosphate

In each adsorption trial, 0.2 g FAA and 100 mL of a phosphate solution were transferred into a flask and adjusted to a pH of 5.0 by the addition of HCl (0.10 M) or NaOH (0.10 M) solutions. The

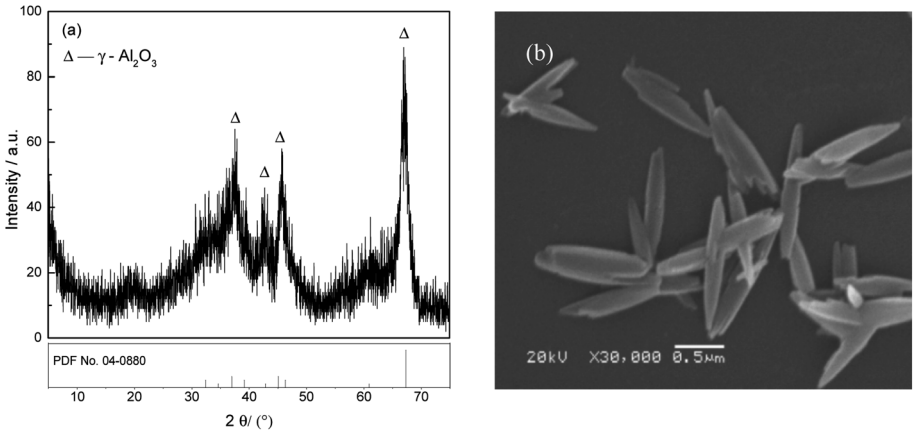

Fig. 1 XRD pattern (a) and SEM image (b) of the FAA $NH_4Al(OH)_2CO_3$ roasted at 450 °C for 180 min.

phosphate removal experiments were carried out at 25 °C while stirring each solution at 150 rpm. The desorption and regeneration of test specimens in dilute NaOH solutions were also performed to verify that the FAA had the properties required for commercial applications. In these trials, a 0.2 g quantity of the used FAA was added to 100 mL of a solution containing NaOH at various concentrations and stirred at 150 rpm for 600 min at a temperature of 25 °C. Sample was sucked from flask to determine concentration of phosphate in solution, adsorption capacity q_t (eqn (1)) and removal rate r (%) (eqn (2)) were then calculated on basis of variation in phosphate concentration.

$$q_t = \frac{(C_0 - C_t)V}{m} \quad (1)$$

$$r\ (\%) = \frac{C_0 - C_t}{C_0} \times 100\% \quad (2)$$

where C_0 and C_t are the initial and t-moment concentration of phosphate in solution (mg L^{-1}), q_t is the t-moment adsorption capacity (mg g^{-1}), m is the mass of the adsorbent (g), and V is solution volume (L).

2.3 Characterization and methods

The phase evolution of alumina-bearing substance was identified by XRD (TTR-III, Rigaku Co., Japan) using Cu kα radiation at a scanning rate of 10° min^{-1}. PSD was finished by using Mastersizer-2000 (Mastersizer-2000, Malvern, UK) after samples were dispersed into deionized water. N_2 adsorption–desorption isotherms were collected at liquid-nitrogen on a Micromeritics ASAP 2020 HD88 (USA). The specific surface area of FAA was calculated by following the multipoint Brunauer–Emmett–Teller (BET) procedures. The Barrett–Joyner–Halenda (BJH) model applied to the desorption branch of the isotherm provided information on the pore size distribution. The morphological structure of the FAA was observed by using SEM (JSM-6360LV, JEOL, Japan).

Meanwhile, the point of zero charge (PZC) was analyzed by using zetasizer Nano S90 (Malvern, UK) at 25 °C. Variation in Al–O coordination of FAA before and after the adsorption of phosphate were analyzed using a Fourier transform infrared spectroscopy (Nicolet 6700 FT-IR, USA) within the range of 500–4000 cm^{-1} and X-ray photoelectron spectrometer (XPS, ESCALAB 250Xi, USA),[26] respectively. In addition, phosphate

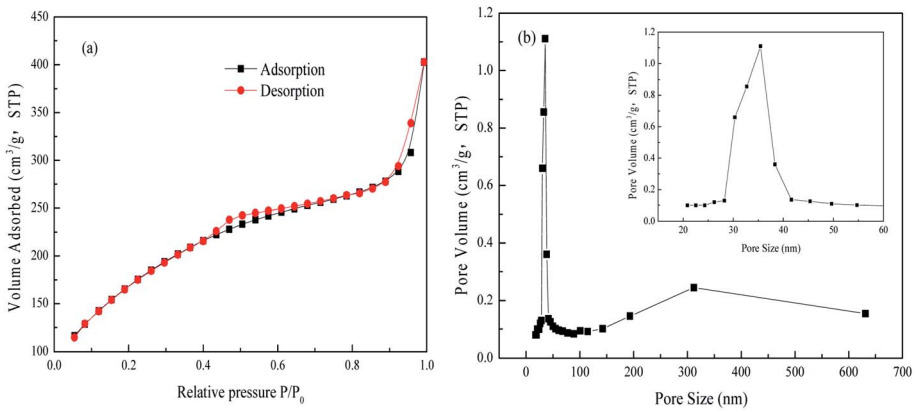

Fig. 2 N_2 adsorption–desorption isotherms (a) and pore diameter distribution curve (b) from the FAA.

concentration was determined by the molybdate blue spectrophotometric method.[18]

3. Results and discussion

3.1 Removal of phosphate with FAA

3.1.1 Effect of pH on phosphate adsorption. The phosphate species in solution (H_3PO_4, $H_2PO_4^-$, HPO_4^{2-}, PO_4^{3-}) determines the interactions with the activated alumina,[15,16] and the ions that are present will in turn be determined by the pH. Fig. 3(a) summarizes the distributions of phosphate anions at various pH based on mass and charge equilibrium. These data indicate that $H_2PO_4^-$ and HPO_4^{2-} will be the dominant species in the pH rang of 4.0 to 10.0, in agreement with literature reports.[27] The effects of pH on phosphate removal by the FAA are presented in Fig. 3(b) and demonstrate that the removal efficiency increased rapidly as the pH was increased from 3.0 to 5.0 and then sharply decreased as the pH was further raised from 6.0 to 10.0. It is apparent from these data that the FAA exhibited relatively high phosphate removal (greater than 69%) over the wide pH range of 3.0 to 10.0, with an especially high efficiency in excess of 95% within the range of 3.5 to 5.0. For these reasons, subsequent trials were performed at a pH of 5.0, at which $H_2PO_4^-$ was the predominant phosphate anion.

3.1.2 Adsorption isotherms. Fig. 4(a) shows the effects of phosphate concentration on the FAA adsorption capacity and removal rate of phosphate. The capacity is seen to have increased rapidly at concentrations below 1100 mg L^{-1} and then slowly increased with further increases in concentration. The maximum adsorption capability was 261.66 mg g^{-1}, which is believed to have been essentially equal to an equilibrium state. In contrast, increases in the phosphate concentration reduced the removal rate. As an example, the phosphate removal decreased from 96.8% to 26.8% as the concentration was increased from 50 to 900 mg L^{-1}, respectively.

An adsorption model that explains this behavior is evidently required to understand the phosphate adsorption mechanism on FAA. Non-linear Langmuir isotherm and Freundlich isotherm were applied to describe the equilibrium adsorption model expressed as follows eqn (3) and (4).[16,17]

$$q_e = \frac{q_{max} \cdot K_L \cdot C_e}{1 + K_L \cdot C_e} \quad (3)$$

$$q_e = K_F \cdot C_e^{1/n} \quad (4)$$

where C_e (mg L^{-1}) and q_e (mg g^{-1}) represent the equilibrium adsorption concentration, equilibrium adsorption capacity, respectively. q_m (mg g^{-1}) stands for the maximum adsorption capacity, and K_L (L mg^{-1}) is the non-linear Langmuir adsorption equilibrium constant. n is a constant in Freundlich adsorption isotherm model, and K_F (mg g^{-1}) (mg L^{-1}) is the Freundlich equilibrium constant.

The data in Fig. 4(a) were fit using non-linear Langmuir and Freundlich isothermal adsorption models, as shown in Fig. 4(b), with R^2 values of greater than 0.99. These results suggest that both monolayer and multilayer adsorption occurred on the surface of the activated alumina. Table 1 provides the maximum adsorption capacities reported for various activated alumina. It is evident that the present FAA, which contained numerous open mesopores (Fig. 2), had the highest capacity for phosphate, even as the fine powder. These data also indicate that the adsorption capacity of such materials does not increase linearly with specific surface area. That is, the adsorption capacity values obtained from the batch experiments may also have been determined by the surface properties and the extent of Al–O coordination in the FAA.

3.1.3 Adsorption kinetics. The effect of contact time on adsorption was examined by fitting the data to a kinetic model. Fig. 5(a) plots the data acquired over time and indicates a rapid increase in adsorption up to 600 min, after which the adsorption increased more slowly and eventually plateaued at approximately 1000 min. The initial rapid phosphate adsorption onto the FAA are mainly attributed to electrostatic physisorption and to the high specific surface area and numerous open mesopores of this material.[28] In contrast, chemisorption might have contributed to the slow increase in phosphate removal after 600 min.[3] It should be noted that over 96% of the original phosphate was captured from a 50 mg L^{-1} solution at a pH of 5.0 after 600 min.

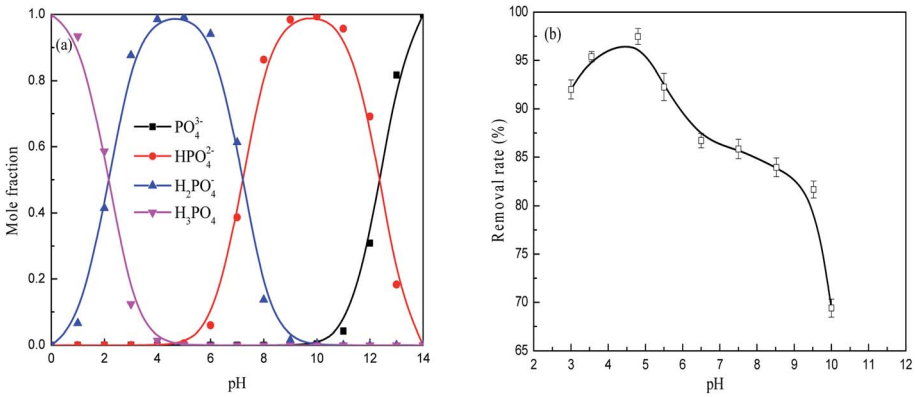

Fig. 3 The phosphate species present in solutions at various pH values (a) and effect of pH on phosphate removal by the FAA (b) 2 g L^{-1} FAA and 100 mL phosphate wastewater, initial phosphate concentration 50 mg L^{-1}, 25 °C, agitation of 150 rpm, time 600 min.

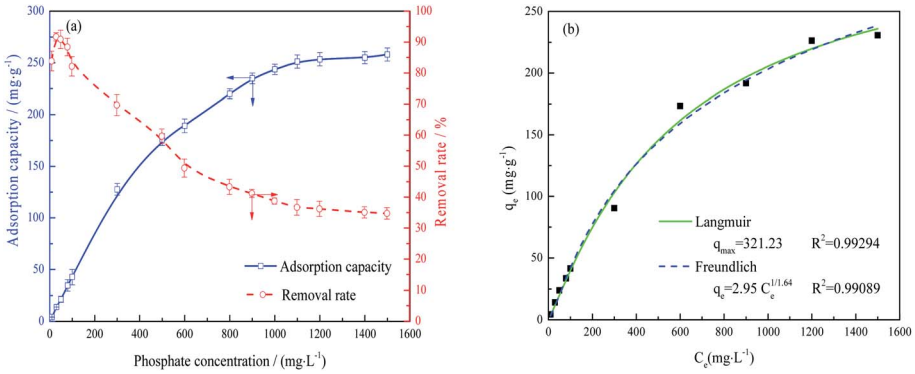

Fig. 4 Adsorption capacity and removal rate of the FAA as functions of phosphate concentration (a) and the experimental data fitted by non-linear Langmuir and Freundlich isothermal adsorption models (b) 2 g L^{-1} FAA and 100 mL phosphate wastewater, pH = 5.0, 25 °C, agitation of 150 rpm, and time 600 min.

Table 1 Phosphate adsorption capacities reported for various materials

Adsorbent	Specific surface area	Adsorption capacity/mg g^{-1}	pH	Ref.
Aluminum oxide	1.1 μm, 295.3 m^2 g^{-1}	30.2	9.7	Kawasaki *et al.*[9]
Nano-alumina	<50 nm, >40 m^2 g^{-1}	6.25	2.0	Mor *et al.*[28]
Commercial Al_2O_3	395.6 nm	14.80	—	Zhang *et al.*[13]
Acid-activated neutralized red mud	—	492.46		Jie *et al.*[16]
Activated aluminum oxide	298.3 m^2 g^{-1}	20.88	—	Xie *et al.*[18]
Activated alumina pellet	Diameters of 2 mm	49.67	—	Choi *et al.*[29]
Zeolite pellet	Diameters of 2 mm	111.49	—	Choi *et al.*[29]
Activated aluminium oxide	0.3–1 mm, 230–300 m^2 g^{-1}	7.9	8.2	Genz *et al.*[30]
Activated alumina	—	53.7	6.4	Shin *et al.*[31]
Al impregnated SBA-15	—	81.9	6.4	Shin *et al.*[31]
Steel-making slag	—	215.7	—	Jha *et al.*[32]
FAA	0.545 μm, 648.02 m^2 g^{-1}	261.66	5.0	This work

Fig. 5(b) demonstrates that the data were in good agreement with the pseudo-second-order model,[33,34] such that fitting the values gave an R^2 of 0.999. This result suggests that chemisorption was the rate-determining step and that various diffusion processes (such as surface, liquid membrane and internal diffusion) were all involved.[35]

3.1.4 Performance of regenerated FAA. FAA samples were regenerated following the adsorption of phosphate and reused to examine the feasibility of adsorbent reuse as a means of reducing costs. Fig. 6(a) and (b) summarize the data from these trials.

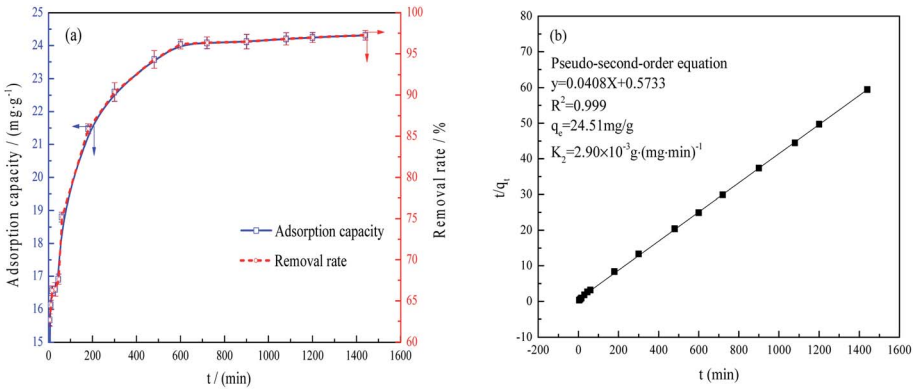

Fig. 5 Phosphate adsorption capacity and removal rate as functions of time (a) and fitting of the data using a pseudo-second-order equation (b) 2 g L^{-1} FAA, and 100 mL phosphate wastewater, phosphate concentration 50 mg L^{-1}, pH = 5.0, 25 °C, agitation of 150 rpm.

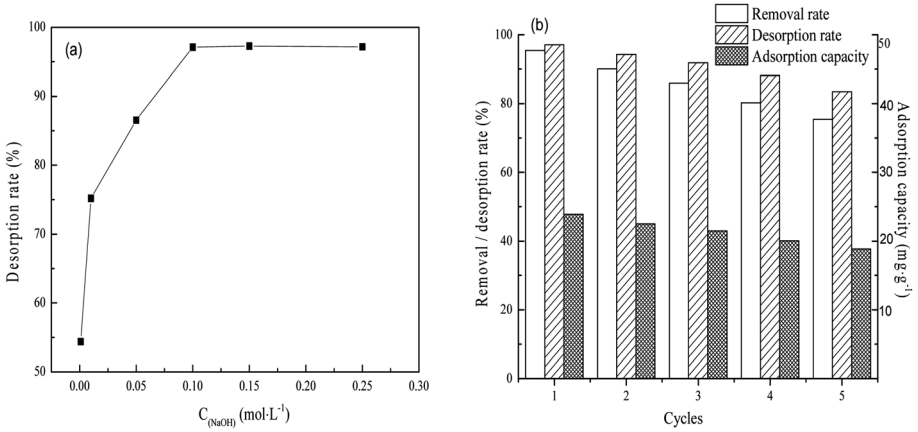

Fig. 6 The desorption rate of the adsorbed phosphate on FAA as a function of NaOH concentration (a) and the phosphate adsorption capacity, removal and desorption rate following repeated reuse of the same FAA specimen (b). Desorption: FAA after removal of phosphate 2 g L^{-1}, temperature 25 °C, time 600 min, agitation rate 150 rpm. Adsorption: regenerated FAA 2 g L^{-1}, initial phosphate concentration 50 mg L^{-1}, pH 5.0 and temperature 25 °C, time 600 min, agitation rate 150 rpm.

As shown in Fig. 6(a), 97.12% of the phosphate could be removed from the FAA after use by immersion in 0.1 mol L^{-1} NaOH. This result is primarily ascribed to the physisorption properties and open pore structure of the FAA (Fig. 2(b)). This high desorption rate implies that the regenerated FAA could be reused with suitable performance and Fig. 6(b) shows the phosphate removal rate, desorption rate and adsorption capacity data during numerous recycling trials with the same sample. After the FAA was regenerated four times, it exhibited a removal rate that was 82% of the initial value. After five cycles, 75.7% of the original adsorption capacity was still obtained. These results confirm that the FAA exhibited excellent performance in terms of phosphate removal.

3.2 Zeta potential and surface structure of the FAA after phosphate adsorption

3.2.1 Variation of zeta potential. Both the physisorption and chemisorption of phosphate would be expected to change the zeta potential of the FAA and so this parameter was used to characterize the surface properties of the material before and after adsorption. The resulting data are plotted in Fig. 7.

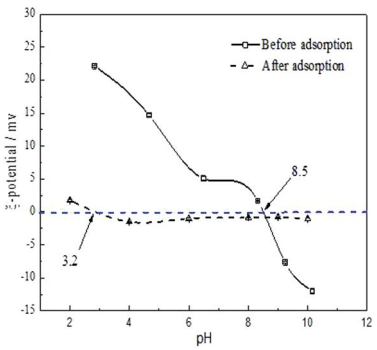

Fig. 7 Zeta potential of the FAA before and after phosphate adsorption as function of pH temperature 25 °C, FAA: 2 g L^{-1} in deionized water.

As shown in Fig. 7, the zeta potential of the FAA decreased with increases in pH both before and after the adsorption of phosphate. The zero charge pH values of the material before and after adsorption were 8.5 and 3.2, respectively. Therefore, reductions in the zeta potential were responsible for the decreased adsorption efficiency at higher pH values seen in Fig. 3(b), meaning that electrostatic interactions decreased or repulsive forces increased. The alumina was observed to have a positive charge at a pH of 5.0 (originating from $Al(OH)_3$ in negative charge) that would be expected to favor the electrostatic adsorption of phosphate anions.[36] The positive charge on the material resulted from the surface protonation of Al(III) atoms in the form of $(O)_nAl(OH)_2^+$ (n = 4, 5 or 6), which was caused by tetra-coordinated AlO_4 or penta-coordinated AlO_5 and saturated hexa-coordinated AlO_6 in the FAA. As a consequence of the phosphate anions adsorbed on the surface of the alumina, the zeta potential of the specimen was remarkably reduced and pH was found to have a minimal effect on zeta potential after adsorption. This finding implies that tetra-coordinated AlO_4 or penta-coordinated AlO_5 in the FAA acted as Lewis acids and both readily reacted with $H_2PO_4^-$ anions at a pH of 5.0, and that the protonation of Al(III) atoms acting as Brønsted acids provided further interactions with these anions.

3.2.2 FTIR spectra. Active sites on the γ-Al_2O_3 surface are believed to contribute to its adsorption capacity, although the relationship between these sites and the Al–O coordination remains unclear. In the present work, FTIR spectroscopy was used to obtain information regarding changes in Al–O bonds before and after the adsorption of phosphate, with the results shown in Fig. 8(a). Protonation of the FAA in solution generated O–H bonds with an associated peak at 3440 cm^{-1} (spectrum #4 in Fig. 8(a)). This peak was much more intense after adsorption compared with before (spectrum #3). The spectrum after adsorption also showed a new peak at 1070 cm^{-1} that was assigned to the stretching vibration of P–O bonds based on the $AlPO_4$ spectrum (spectrum #1). These data establish that the chemisorption of phosphate occurred,[37] reducing removal

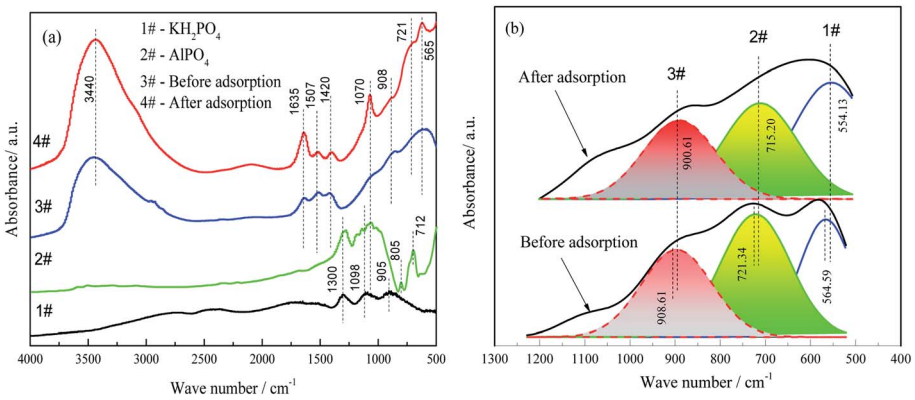

Fig. 8 FTIR spectra of the FAA before and after phosphate adsorption (spectra of KH_2PO_4 and $AlPO_4$ are included as references) (a) and peak fitting of the spectra within the range of 500–1200 cm^{-1} (b). (a) 1# – KH_2PO_4; 2# – $AlPO_4$; 3# – before adsorption; 4# – after adsorption; (b) 1# – 554 cm^{-1} of Al–O stretch (AlO_6); 2# – 715 cm^{-1} of Al–O stretch (AlO_4); 3# – 900 cm^{-1} of Al–O stretch (AlO_4).

efficiency of the regenerated FAA (Fig. 6(b)). The peaks at 554, 715 and 900 cm^{-1} generated by the material before adsorption were related to Al–O bonds in the alumina and were shifted to 564.59, 721.34 and 908.61 cm^{-1} after exposure to the phosphate solution. These variations are primarily ascribed to physisorption.

Furthermore, AlO_4 and less than 5% AlO_5 coexist in γ-Al_2O_3 compared with α-Al_2O_3 which is made of AlO_6.[38,39] The AlO_4 sites primarily determined the degree of chemisorption by the FAA. Fig. 8(b) shows the results of FTIR peak fittings at 554, 715 and 900 cm^{-1} while Table 2 summarizes the variations in the areas of the peaks related to AlO_4 and AlO_6.

The peaks at 554.13, 715.20 and 900.61 cm^{-1} were assigned to the stretching vibrations of Al–O bonds in AlO_6 and AlO_4, respectively.[42] The adsorption of phosphate by the FAA decreased the AlO_4 peak area but increased that of the AlO_6 peak. These data suggest that the reaction of AlO_4 sites with the $H_2PO_4^-$ anions, electrostatic interaction of AlO_4 and AlO_6 after protonation with $H_2PO_4^-$, respectively.

3.2.3 XPS spectra. Additional information related to Al–O coordination states on the FAA surface was acquired by obtaining XPS spectra to monitor variations in AlO_4 and AlO_6 sites before and after phosphate adsorption. Peak fitting of the Al 2p spectra identified peaks related to AlO_4 (74.13 eV) and AlO_6 (75.43 eV).[14,43] The results of these analyses are presented in Fig. 9 and Table 3.

Spectrum #2 in Fig. 9(a) demonstrates the presence of elemental phosphorous on the FAA surface after adsorption based on the action of AlO_4 Lewis acid sites that reacted with $H_2PO_4^-$ to generate Al–O–P groups (see also spectrum #4) in Fig. 8(a).[44] The results in Fig. 9(b) and Table 3 show that the AlO_6 peak area increased by 15% while the AlO_4 peak area decreased by 15% after adsorption, which is consistent with the FTIR results in Fig. 8(b) and Table 2. These data provide evidence that physisorption was primarily responsible for the removal of phosphate along with some chemisorption. Both the FTIR and XPS results also show differences in the mass-based proportions of AlO_4 and AlO_6. From these differences, it is evident that phosphate anions were mainly adsorbed on the FAA surface, meaning that the high specific surface area and open mesopores of this material contributed to its high adsorption capacity.

The P 2p XPS spectrum obtained from the FAA after phosphate adsorption is shown in Fig. 9(c) and summarized in Table 3. The peak at a binding energy of 134.2 eV was assigned to $H_2PO_4^-$ and demonstrates the electrostatic interaction between this anion and $(O)_nAl(OH)_2^+$ (n = 4, 5 or 6) sites acting as Brønsted acids, by which physisorption took place.[12] The peak

Table 2 FTIR peak assignments and variations in peak areas before and after phosphate adsorption[a]

No.	Band assignment	ν[40,41] (cm^{-1})	Peak W_1 before adsorption (cm^{-1})	Peak W_2 after adsorption (cm^{-1})	$\Delta W = W_2 - W_1$ (cm^{-1})	Area (A_1) before adsorption (%)	Area (A_2) after adsorption (%)	$\Delta A = A_1 - A_2$ (%)
1#	Al–O stretch (AlO_6)	523	564.59	554.13	10.46	25.27	33.31	+8.04
2#	Al–O stretch (AlO_4)	734	721.34	715.20	6.14	43.22	36.44	−6.78
3#	Al–O stretch (AlO_4)	852	908.61	900.61	8.00	31.51	30.25	−1.26

[a] W – wave number, ΔW – difference of the peak wave number; ΔA – difference of the peak area.

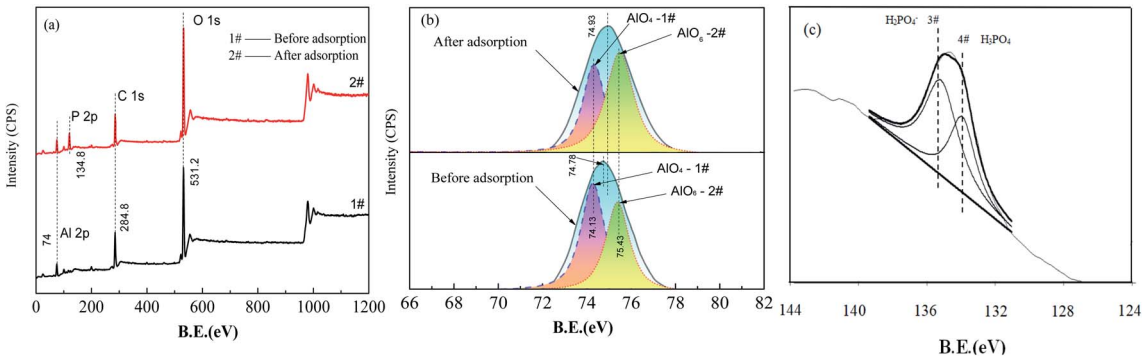

Fig. 9 XPS survey spectra obtained from the FAA before and after phosphate adsorption (a) and the results of peak fitting within the range of 72–78 eV (b) and the P 2p region after phosphate adsorption within the range of 133.4–134.2 eV (c). (a) 1# – before adsorption; 2# – after adsorption; (b) 1# – 74.13 eV of Al–O stretch (AlO_4); 2# – 75.43 eV of Al–O stretch (AlO_6); (c) 3# – $H_2PO_4^-$, 134.2 eV; 4# – H_3PO_4,133.4 eV.

Table 3 XPS peak assignments and peak areas before and after phosphate adsorption[a]

No.	Al 2p/P 2p	Position (eV)	Position before adsorption (eV)	Position after adsorption (eV)	$\Delta W = W_2 - W_1$ (eV)	Area (A_1) before adsorption (%)	Area (A_2) after adsorption (%)	$\Delta A = A_1 - A_2$ (%)
1#	Al–O (AlO_4)	74.13	74.38	74.36	0.02	57.48	42.48	−15.00
2#	Al–O (AlO_6)	75.43	75.48	75.55	0.07	42.52	57.52	+15.00
3#	$H_2PO_4^-$	134.2	—	134.19	0.01	—	61.83	—
4#	H_3PO_4 or $AlPO_4$	133.4	—	135.23	1.83	—	38.17	—

[a] W – peak position, ΔW – difference of the peak position; ΔA – difference of the peak area.

at 133.4 eV corresponds to H_3PO_4 or $AlPO_4$ and resulted from the chemisorption of $H_2PO_4^-$ on AlO_4 sites.[45,46]

3.2.4 Adsorption mechanism. In the present work, FAA prepared from an industrial sodium aluminate solution based on phase evolution from $Al(OH)_3$ and $NH_4Al(OH)_2CO_3$ showed exceptional adsorption capacity. On the basis of the present results, the mechanism by which phosphate was removed from solution by the FAA is presented in Fig. 10.

The plentiful open mesopores in the FAA provided a high specific surface area and the γ-Al_2O_3 contained numerous AlO_4 units acting as Lewis acids. The positive charges on the alumina also promoted interactions between the FAA surface and phosphate anions, while the formation of $AlPO_4$ improved the

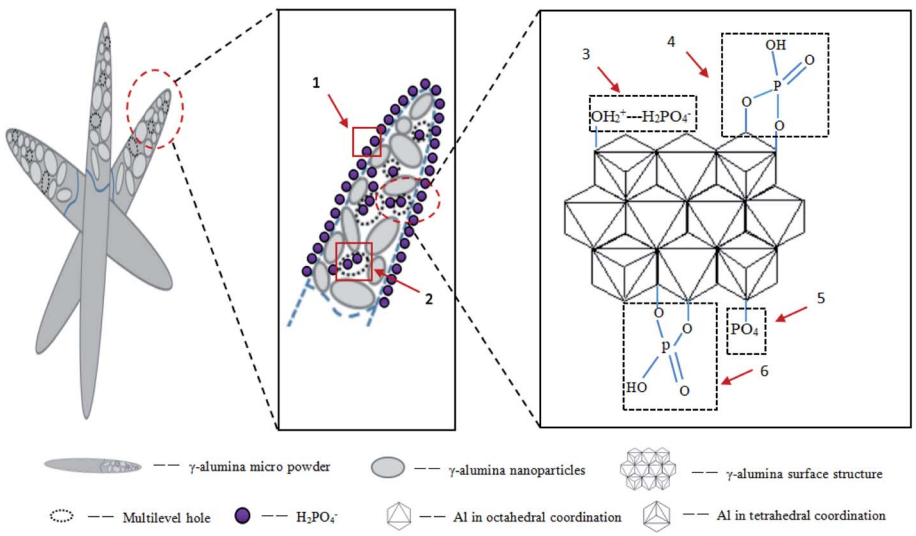

Fig. 10 The diagram showing the phosphate adsorption mechanism on FAA. (1) surface diffusion, (2) internal diffusion, (3) physisorption with AlO_4 after protonation, (4) physisorption with AlO_4, (5) chemisorption with AlO_4 after formation of $AlPO_4$, (6) physisorption with AlO_6.

adsorption of phosphate. All these phenomena synergistically contributed to the high adsorption capacity of the FAA. Fig. 10 shows that anion diffusion over the FAA surface and through a liquid membrane, as well as internal diffusion, were responsible for the removal of phosphate (see also Fig. 5(b)). In future work, the effects of other anions on phosphate removal and degradation of the FAA after regeneration will be studied.

4. Conclusions

(1) FAA having a $d(50)$ value of 0.545 μm was prepared from an industrial sodium aluminate solution by the phase transition of $Al(OH)_3$ and $NH_4Al(OH)_2CO_3$. The FAA comprised small nanocrystallites containing numerous open mesopores and so had a large specific surface area of 648.02 $m^2\ g^{-1}$. $H_2PO_4^-$ was found to be the predominant phosphate anion in solution at a pH of 5.0 and the zeta potential of the FAA was determined to decrease significantly with increases in pH before the adsorption of phosphate. After phosphate adsorption, pH had a minimal effect on the zeta potential of the material.

(2) Increases in the phosphate concentration or extending the adsorption duration improved the extent of phosphate uptake by the FAA. The maximum adsorption capacity of the material was 261.66 mg g^{-1} from a solution having a phosphate concentration of 1000 mg L^{-1} at a pH of 5.0. The phosphate adsorption data could be accurately fit using non-linear Langmuir and Freundlich isotherm models assuming monolayer and multilayer adsorption. More than 96% of the phosphate in a 50 mg L^{-1} solution could be adsorbed and the adsorption kinetics followed a pseudo-second-order model with chemisorption as the rate-determining step. Regenerated FAA continued to exhibit high performance after immersion in a dilute NaOH solution.

(3) Phosphate removal was primarily *via* physisorption although some chemisorption also occurred. The number of tetra-coordinated AlO_4 sites in the FAA was greatly decreased following the adsorption of $H_2PO_4^-$ while the concentration of hexa-coordinated AlO_6 sites was increased. The high specific surface area, numerous open mesopores and plentiful tetra-coordinated AlO_4 sites on the FAA all contributed in a synergistic manner to its high adsorption capacity.

Conflicts of interest

On behalf of my co-authors, I declare that this work has neither been published previously nor under consideration for publication elsewhere. All authors have revised the manuscript and approved to submit to your journal. Meanwhile, there are no conflicts of interest.

Acknowledgements

The authors gratefully acknowledge the financial support from the National Natural Science Foundation of China (No. 51874366).

References

1 S. Tian, P. Jiang, P. Ning and Y. Su, *Chem. Eng. J.*, 2009, **151**(1), 141–148.
2 T. Li, T. Liao, X. Su, X. Yu, B. Han, Y. Zhu and Y. Zhang, *Water Res. Technol.*, 2018, **4**, 1671–1684.
3 J. Diao, L. Shao, D. Liu, Q. Yong, W. Tan, W. Liang and B. Xie, *JOM*, 2018, **70**(10), 1–6.
4 Z. Zha, Y. Ren, S. Wang, Q. Zhuang, Y. Lei, P. Cheng, Y. Han and M. Wang, *RSC Adv.*, 2018, **8**(34), 19326–19334.
5 I. W. Almanassra, G. Mckay, V. Kochkodan, M. A. Atieh and A. A. Tareq, *J. Chem. Eng.*, 2021, **409**, 128211.
6 C. Lu, K. Klementiev, T. Hassenkam, W. Qian, J. Ai and H. Hansen, *J. Chem. Eng.*, 2021, **422**(23), 130009.
7 N. M. Del, C. Galindo, R. Barillon, E. Halter and B. Madé, *J. Colloid Interface Sci.*, 2010, **342**(2), 437–444.
8 X. F. Hu, Y. Q. Liu, Z. Tang, G. C. Li, R. Y. Zhao and C. G. Liu, *Mater. Res. Bull.*, 2012, **47**(12), 4271–4277.
9 N. Kawasaki, F. Ogata, K. Takahashi, M. Kabayama, K. Kakehi and S. Tanada, *J. Health Sci.*, 2008, **54**(3), 324–329.
10 C. L. Lu, J. G. Lv, L. Xu, X. F. Guo, W. H. Hou, Y. Hu and H. Huang, *Nanotechnol*, 2009, **20**(21), 215604.
11 G. H. Liu, G. Y. Wu, W. Chen, X. B. Li, Z. H. Peng, Q. S. Zhou and T. G. Qi, *Hydrometallurgy*, 2018, **176**, 253–259.
12 S. Mor, K. Chhoden, P. Negi and K. Ravindra, *Environmental Nanotechnology Monitoring and Management*, 2016, **7**, 15–23.
13 L. Zhang, S. Hong, J. He, F. Gan and Y. S. Ho, *Clean: Soil, Air, Water*, 2010, **38**(9), 831–836.
14 E. W. Shin, J. S. Han, M. Jang, S. H. Min, J. K. Park and R. M. Rowell, *Environ. Sci. Technol.*, 2004, **38**(3), 912–917.
15 Ahamad, R. Singh, I. Baruah, H. Choudhury and M. R. Sharma, *Groundwater for Sustainable Development*, 2018, **7**, 452–458.
16 Jie, X. Cong, P. Zhang, E. Hoffmann, G. M. Zeng, Y. Liu, W. Fang, Y. Wu and H. B. Zhang, *Appl. Surf. Sci.*, 2015, **356**(30), 128–134.
17 K. Zhang, L. V. Dyk, D. He, J. Deng and H. Zhao, *Green Process. Synth.*, 2021, **10**(1), 349–360.
18 J. Xie, Y. Lin, C. Li, D. Wu and H. Kong, *Powder Technol.*, 2015, **269**, 351–357.
19 S. Gypser, F. Hirsch, A. M. Schleicher and D. Freese, *J. Environ. Sci.*, 2018, **70**(8), 175–189.
20 D. Kang, X. Yu, M. Ge, M. Lin, X. Yang and Y. Jing, *Chem. Eng. J.*, 2018, **345**, 252–259.
21 G. Y. Wu, G. H. Liu, X. B. Li, Z. H. Peng, Q. S. Zhou and T. G. Qi, *RSC Adv.*, 2019, **9**, 5628–5638.
22 W. Q. Huang, G. H. Liu, T. G. Qi, X. B. Li, Q. S. Zhou and Z. H. Peng, *CrystEngComm*, 2020, **22**, 6983.
23 C. L. Lu, J. G. Lv, L. Xu, X. F. Guo, W. H. Hou, Y. Hu and H. Huang, *Nanotechnol*, 2009, **20**(21), 215604.
24 X. Fei and W. Li, *Mater. Lett.*, 2010, **64**, 1858–1860.
25 E. Im, H. J. Seo, I. K. Da, H. C. Dong and M. D. Geon, *J. Chem. Eng.*, 2021, **416**(19), 129147.
26 W. Q. Huang, G. H. Liu, X. B. Li, T. G. Qi, Q. S. Zhou and Z. H. Peng, *J. Alloys Compd.*, 2020, **824**, 153905.

27 X. Yang, D. Wang, Z. Sun and H. Tang, *Colloids Surf., A*, 2007, **297**(1–3), 84–90.
28 S. Mor, K. Chhoden, P. Negi and K. Ravindra, *Environ. Nanotechnology, Monitoring & Management*, 2016, **7**, 15–23.
29 J. W. Choi, S. Y. Lee, S. H. Lee, J. E. Kim, K. Y. Park, D. J. Kim and S. W. Hong, *Water, Air, Soil Pollut.*, 2012, **223**(6), 2881–2890.
30 A. Genz, A. Kornmüller and M. Jekel, *Water Res.*, 2004, **38**(16), 3523–3530.
31 E. W. Shin, J. S. Han, M. Jang, S. H. Min, J. K. Park and R. M. Rowell, *Environ. Sci. Technol.*, 2004, **38**, 912–917.
32 V. K. Jha, Y. Kameshima, A. Nakajima and K. Okada, *J. Hazard. Mater.*, 2008, **156**(1–3), 156–162.
33 M. Özacar, *Adsorption J. international adsorption Soc.*, 2003, **9**(2), 125–132.
34 B. Kostura, H. Kulveitovã and J. Lesko, *Water Res.*, 2005, **39**, 1795–1802.
35 M. Pan, X. Lin, J. Xie and X. Huang, *RSC Adv.*, 2017, **7**, 4492–4500.
36 X. Yang and B. Al-Duri, *J. Colloid Interface Sci.*, 2005, **287**, 25–34.
37 S. Gypser, F. Hirsch, A. M. Schleicher and D. Freese, *J. Environ. Sci.*, 2018, **70**, 178–192.
38 L. H. Chagas, G. Carvalho, R. Gil, S. S. X. Chiaro, A. A. Leitão and R. Diniz, *Mater. Res. Bull.*, 2014, **49**, 216–222.
39 C. Pecharromán, I. Sobrados, J. E. Iglesias, T. Gonzalez-Carreno and J. Sanz, *J. Phys. Chem. B*, 1999, **103**, 6160–6170.
40 T. Meher, A. K. Basu and S. Ghatak, *Ceram. Int.*, 2005, **31**, 831–838.
41 P. Tarte, *Spectrochim. Acta, Part A*, 1967, **23**, 2127–2143.
42 T. T. Zheng, Z. X. Sun, X. F. Yang and A. Holmgren, *J. Chem. Central*, 2012, **6**(1), 26–36.
43 N. Y. Zhu, T. M. Yan, J. Qiao and H. L. Cao, *Chemosphere*, 2016, **164**, 32–40.
44 Roy, D. Wisser, M. Rivallan, M. C. Valero, T. Corre, O. Delpoux, G. D. Pirngruber and G. Lefèvre, *J. Phys. Chem. C*, 2021, **125**, 10909–10918.
45 Y. Yao, B. Gao, J. Chen and L. Yang, *Environ. Sci. Technol.*, 2013, **47**, 8700–8708.
46 A. Hühn, D. Wisser, M. C. Valero, T. Roy, M. Rivallan, L. Catita, A. Lesage, C. Michel and P. Raybaud, *ACS Catal.*, 2021, **11**, 11278–11292.